JACS
JOURNAL OF THE AMERICAN CHEMICAL SOCIETY
Article
pubs.acs.org/JACS

Metal–Organic Framework Derived Hybrid Co_3O_4-Carbon Porous Nanowire Arrays as Reversible Oxygen Evolution Electrodes

Tian Yi Ma,[†] Sheng Dai,[†] Mietek Jaroniec,[‡] and Shi Zhang Qiao*[,†]

[†]School of Chemical Engineering, The University of Adelaide, Adelaide, South Australia 5005, Australia
[‡]Department of Chemistry and Biochemistry, Kent State University, Kent, Ohio 44240, United States

Supporting Information

ABSTRACT: Hybrid porous nanowire arrays composed of strongly interacting Co_3O_4 and carbon were prepared by a facile carbonization of the metal–organic framework grown on Cu foil. The resulting material, possessing a high surface area of 251 m^2 g^{-1} and a large carbon content of 52.1 wt %, can be directly used as the working electrode for oxygen evolution reaction without employing extra substrates or binders. This novel oxygen evolution electrode can smoothly operate in alkaline solutions (e.g., 0.1 and 1.0 M KOH), affording a low onset potential of 1.47 V (vs reversible hydrogen electrode) and a stable current density of 10.0 mA cm^{-2} at 1.52 V in 0.1 M KOH solution for at least 30 h, associated with a high Faradaic efficiency of 99.3%. The achieved ultrahigh oxygen evolution activity and strong durability, with superior performance in comparison to the state-of-the-art noble-metal/transition-metal and nonmetal catalysts, originate from the unique nanowire array electrode configuration and in situ carbon incorporation, which lead to the large active surface area, enhanced mass/charge transport capability, easy release of oxygen gas bubbles, and strong structural stability. Furthermore, the hybrid Co_3O_4-carbon porous nanowire arrays can also efficiently catalyze oxygen reduction reaction, featuring a desirable four-electron pathway for reversible oxygen evolution and reduction, which is potentially useful for rechargeable metal–air batteries, regenerative fuel cells, and other important clean energy devices.

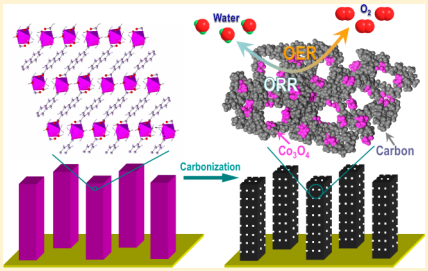

1. INTRODUCTION

Growing energy demands have stimulated a considerable interest in alternative energy conversion and storage systems such as metal–air batteries, water splitting devices, and fuel cells, which are all closely associated with a core process, an oxygen evolution reaction (OER) that is initiated at the boundary of multiple phases (solid, liquid, gas).[1] To rationally design the reaction interface for an OER, an optimal electrode structure involving high-performance catalysts is essential in reducing the overpotential, promoting the reaction kinetics, and enhancing the specific activity for OER, thus improving the energy efficiency.[2] However, most of the reported OER electrocatalysts, such as noble-metal (Ir, Ru),[3] transition-metal (Co, Mn, Ni, Fe, etc.)[4] and nonmetal catalysts (graphitic carbon nitrides, N-doped graphitic carbons, etc.),[5] are generally prepared in the form of thin films or particle agglomerates coated onto glassy carbon, nickel foam, or other conductive substrates. In most cases, these fabrication techniques require time-consuming film casting or coating procedures with the assistance of polymeric binders, which result in uncontrolled microstructure of the obtained electrodes featuring limited catalytically active surface areas that are unfavorable for electron conductivity and multiphase reactant/product transport during OER (e.g., OH^- in the liquid phase, O_2 in the gas phase). Also, the easy peeling of the coated catalysts from the electrodes during evolution of a large amount of O_2 greatly impairs their electrocatalytic activity and shelf life.[6] Thus, the development of alternative electrode configurations for efficiently catalyzed OER with high activity and strong long-term stability is urgently needed.

Recently, well-aligned nanowire arrays with catalytically active components directly grown on the current collectors have been considered as a new generation of highly effective electrodes, due to their intrinsic advantages.[7] The open space within nanowire arrays facilitates the electrolyte penetration and diffusion of ionic species, allowing high utilization efficiency of active species. The direct contact of nanowire arrays with the underlying conductive current collectors and their strong binding ensure good electrical conductivity between them, as well as high structural stability of the obtained electrodes.[6b,c,7,8] Thus, these electrodes show great potential for direct use in electrochemical cells, and they are particularly beneficial for OER that involves continuous evolution of O_2 gas.[1,3−5]

Nevertheless, the use of nanowire arrays for electrocatalytic OER is still in its infancy. Only a few illustrations, including $Zn_xCo_{3-x}O_4$ and $Ni_xCo_{3-x}O_4$ nanowire arrays grown on Ti foils,[9] Co_3O_4 nanowire arrays grown on stainless steel meshes,[10] and Ni-substituted Co_3O_4 nanowire arrays grown on Ni foams,[11] have been reported, all focusing on Co_3O_4-based spinel materials due to their good catalytic activity and corrosion stability toward electrochemical OER in alkaline media.[12] Their fabrication unexceptionally involved nucleation

Received: August 15, 2014
Published: September 12, 2014

   dx.doi.org/10.1021/ja5082553 | J. Am. Chem. Soc. 2014, 136, 13925−13931

and growth of inorganic precursors on certain substrates and was limited to pure metal oxides.[9−11] However, semiconducting metal oxide nanowires having the length of several micrometers do not ensure a continuous pathway for electron transport along them.[7] Also, the mass transport and accessible catalytically active sites associated with individual nanowires are limited due to the low porosity and relatively small surface area of the nanowires.[9−11] Therefore, further improvement of this type of electrode is highly desirable, especially through increasing the electrical conductivity of single nanowires by elemental doping or other methods and through introducing accessible pores into the nanowires.

To achieve these goals, we have designed the first hybrid Co_3O_4-carbon porous nanowire arrays (denoted as Co_3O_4C-NA), which are prepared by carbonization of the metal−organic framework (MOF) directly grown on Cu foil under a N_2 atmosphere. The periodic arrangement of metal nodes and organic motifs in MOF scaffolds leads to a homogeneous distribution of metal oxide nanoparticles and in situ formed carbon species. Our purpose is to accomplish better catalytic performance of the hybrid nanowire array electrode by combining distinctive properties of metal oxide and carbon components and taking advantage of their uniform distribution and synergy.[13] Herein, the use of a Co-based MOF as the precursor represents a facile way of obtaining Co_3O_4C-NA with high surface area and large carbon content. Remarkably, Co_3O_4C-NA not only exhibits better oxygen evolution activity and stronger durability in comparison to most of the highly active noble-metal/transition-metal and nonmetal catalysts reported to date but also efficiently catalyzes the reverse oxygen reduction reaction (ORR). Its outstanding activity can be attributed to the large active surface area, favorable charge, and mass transport in the stable nanowire array electrode structure.

2. RESULTS AND DISCUSSION

2.1. Catalyst Synthesis and Characterization. The hybrid Co_3O_4-carbon porous nanowire arrays were synthesized from a Co-naphthalenedicarboxylate MOF with a layered crystalline structure used as the precursor (Scheme 1), which was directly grown on Cu foil through a low-temperature (80 °C) hydrothermal process. Next, the inorganic and organic components in the MOF were converted respectively into Co_3O_4 and carbon via carbonization under a N_2 atmosphere, which resulted in the formation of hybrid nanowires with simultaneously generated pores inside.

Scheme 1. Fabrication of Hybrid Co_3O_4-Carbon Porous Nanowire Arrays

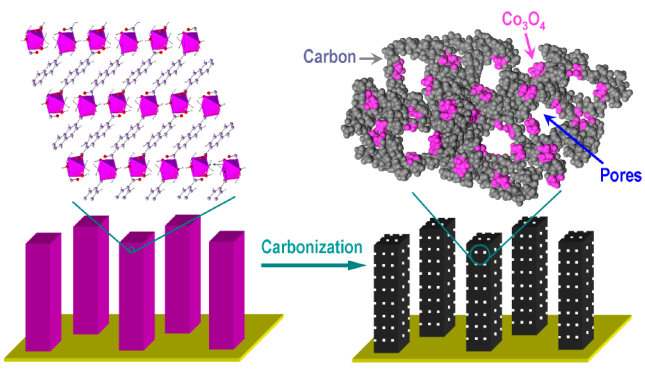

Nanowire arrays of Co_3O_4C-NA (scanning electron microscopy (SEM), Figure 1a,b), preserving the morphology of the

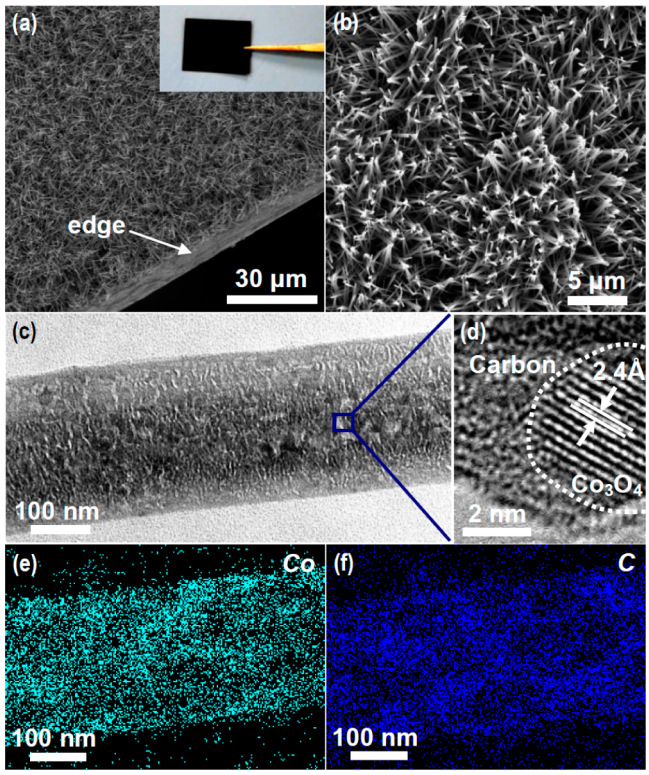

Figure 1. (a, b) SEM, (inset in panel a) optical image, (c) TEM image, (d) HRTEM image, and (e, f) EDS elemental mapping images of Co_3O_4C-NA.

Co-based MOF (Figure S1, Supporting Information), grow on the surface of the Cu foil, the color of which changes to black (Figure 1a, inset). A single nanowire with a smooth surface and a diameter of ∼250 nm is observed in the transmission electron microscopy (TEM) image (Figure 1c). Nanowires obtained with high yield and without the presence of morphologically different particles and their smooth surface indicate that all Co_3O_4 and carbon species are well integrated inside them with a negligible amount of isolated Co_3O_4 nanocrystals. Numerous slitlike pores visible throughout the nanowire are preferably generated via deterioration and carbonization of the alternating organic naphthalene layers,[13] which agrees well with the layered crystalline structure of the MOF (Figure S2, Supporting Information). The high-resolution transmission electron microscopy (HRTEM) image (Figure 1d) presents apparently different domains of amorphous carbon and crystalline Co_3O_4, with a clearly identified lattice fringe space of 2.4 Å corresponding to the (311) plane of the cubic Co_3O_4 spinel phase. Notably, Co species catalyze the formation of partially graphitized carbon on the surface of Co_3O_4. The HRTEM observation is also consistent with the uniform dispersion of Co and C elements in Co_3O_4C-NA (energy dispersive X-ray spectroscopy (EDS) elemental mapping image, Figure 1e,f), together verifying the homogeneous distribution of closely interconnected Co_3O_4 and carbon species.

The multiple peaks on the X-ray diffraction (XRD) pattern of the Co-based MOF used (inset in Figure 2a) well match those of the typical crystalline structure of $Co(C_{12}H_6O_4)$-$(H_2O)_4$,[14] without detectable peaks from cobalt oxides. After

dx.doi.org/10.1021/ja5082553 | J. Am. Chem. Soc. 2014, 136, 13925−13931

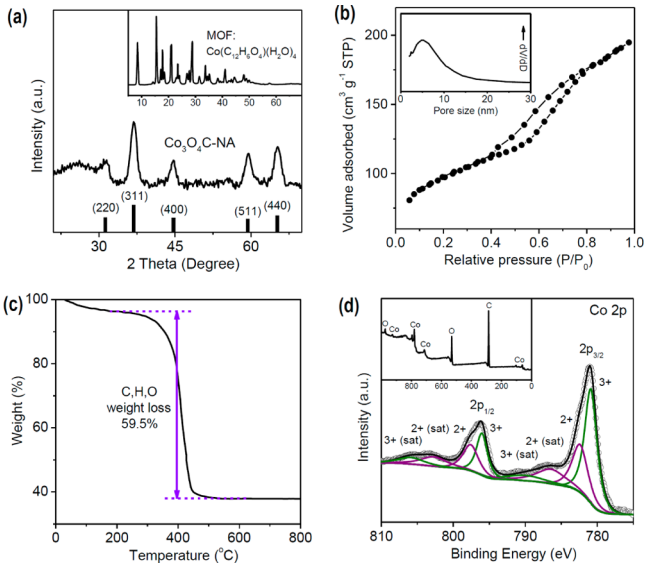

Figure 2. (a) XRD patterns of Co_3O_4C-NA and (inset) the MOF used as the precursor. (b) N_2 adsorption isotherm and (inset) the corresponding pore size distribution of Co_3O_4C-NA. (c) TG curve of Co_3O_4C-NA. (d) High-resolution XPS spectrum of the Co 2p core level and (inset) XPS survey spectrum of Co_3O_4C-NA.

carbonization, Co_3O_4C-NA exhibits the cubic spinel-phase structure (JCPDS No. 43-1003) with a broad shoulder peak in the range 20−30° (2θ), which originates from the amorphous carbon species homogeneously distributed in nanowires that are formed in situ during carbonization process (Figure 2a), as evidenced by HRTEM and EDS. The N_2 adsorption isotherm recorded on Co_3O_4C-NA resembles type IV with an H3 type hysteresis loop (Figure 2b), commonly observed for materials with slitlike mesopores,[15] which agrees well with TEM observations and the layered crystalline structure of the MOF used. Correspondingly, one peak centered at ∼5 nm is found in the pore size distribution curve. Also, Co_3O_4C-NA displays a large surface area of 251 $m^2\ g^{-1}$, which is much higher than that of the Co-based MOF used (Figure S3, Supporting Information) and other reported nanowire arrays prepared by inorganic precursors (up to ∼100 $m^2\ g^{-1}$),[7,9−11] indicating the superiority of our proposed method for creating highly porous hybrid nanowires from MOF via the carbonization process.

The hybrid nature of nanowire arrays was further confirmed by thermogravimetric analysis (TG, Figure 2c). In addition to the 3% weight loss below 200 °C due to the adsorbed water and gases, the weight loss of 59.5% in Co_3O_4C-NA between 200 and 500 °C is ascribed to the combustion of carbon species with some surface-bonded oxygen-containing functional groups, which is consistent with the elemental analysis showing a carbon content of 52.1 wt %. X-ray photoelectron spectra (XPS) indicate that Co_3O_4C-NA contains Co, C, and O elements without other impurities, and the best deconvolution of the Co 2p profile was achieved with the assumption of eight species, including two pairs of spin−orbit doublets indicating the coexistence of Co^{2+} and Co^{3+} and their four shakeup satellites (denoted as "sat", Figure 2d).[16] In comparison to the XPS peak centered at 780.1 eV assigned to Co $2p_{3/2}$ of pure Co_3O_4 (Figure S4, Supporting Information), the shift of the corresponding peak of Co_3O_4C-NA to 781.2 eV implies the close assembly and strong interaction between Co_3O_4 and carbon, resulting in the impaired electron density of Co atoms in Co_3O_4C-NA.[17] Therefore, TEM, EDS, and XPS demonstrate homogeneously dispersed and well-interacting nanocrystalline Co_3O_4 and conductive carbon species in Co_3O_4C-NA, which is desired for high-performance electrocatalysts.

2.2. Oxygen Evolution Activity. Sizable and shapeable electrodes can be prepared by simply tailoring the Cu foil, and the obtained Co_3O_4C-NA grown on Cu foil can be directly used as the working electrode for OER (Figure 3a inset; Figure

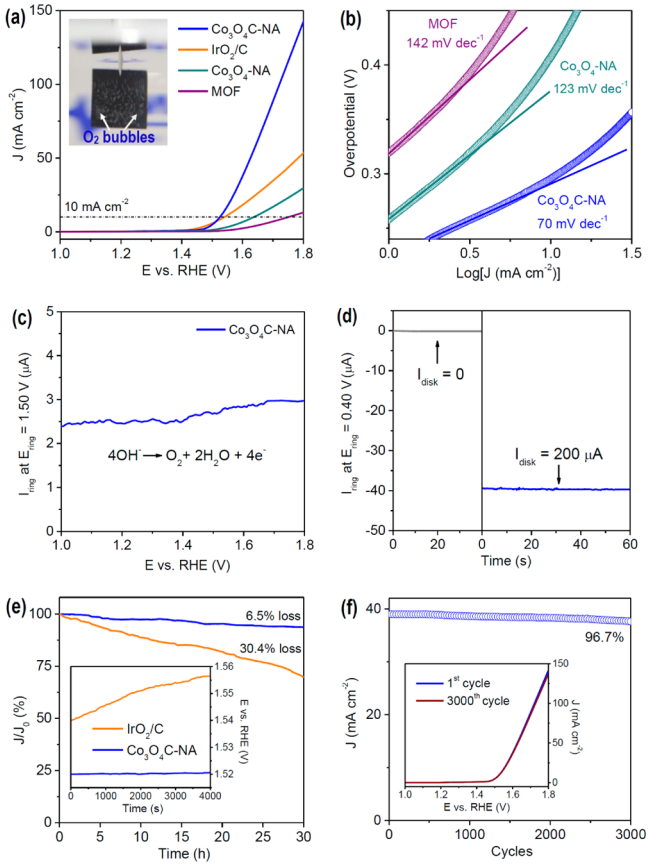

Figure 3. (a) Polarization curves and (b) Tafel plots of Co_3O_4C-NA, IrO_2/C, Co_3O_4-NA, and the MOF in an O_2-saturated 0.1 M KOH solution (scan rate 0.5 mV s^{-1}). Inset in (a): optical image of Co_3O_4C-NA directly used as the OER electrode operating at 1.70 V with generated bubbles on the surface indicating the formation of O_2 gas. (c) Ring current of Co_3O_4C-NA on an RRDE (1500 rpm) in O_2-saturated 0.1 M KOH solution (ring potential 1.50 V). (d) Ring current of Co_3O_4C-NA on an RRDE (1500 rpm) in N_2-saturated 0.1 M KOH solution (ring potential 0.40 V). (e) Chronoamperometric response at a constant potential of 1.52 V ($E_{j=10}$). Inset in (e): chronopotentiometric response at a constant current density of 10.0 mA cm^{-2} of Co_3O_4C-NA in comparison to that of IrO_2/C. (f) Plot of the current density at 1.60 V recorded from the polarization curve of Co_3O_4C-NA vs the cycle number. Inset in panel f: polarization curves of Co_3O_4C-NA before and after 3000 potential cycles (scan rate 100 mV s^{-1}).

S5 and Video S1, Supporting Information) without employing extra substrates (e.g., glassy-carbon electrode) or binders (e.g., Nafion). A slow scan rate (0.5 mV s^{-1}) was applied during the OER test to minimize the capacitive current. Since Co_3O_4 nanocrystals may partially dissolve in acidic solutions such as those of H_2SO_4, alkaline eletrolytes (0.1 and 1.0 M KOH) are preferred for the catalyst studied and were examined in this work. The Cu foil exhibits negligible catalytic activity, as shown

dx.doi.org/10.1021/ja5082553 | J. Am. Chem. Soc. 2014, 136, 13925−13931

in the polarization curve conducted in 0.1 M KOH solution (Figure S6, Supporting Information), and the Co-based MOF also displays low OER response with a high onset potential at ~1.55 V vs the reversible hydrogen electrode (RHE; Figure 3a), while the anodic current recorded on Co_3O_4C-NA renders a sharp onset potential at ~1.47 V with greatly enhanced OER current, indicating that the compositional transformation of the MOF to the Co_3O_4-carbon hybrid can significantly improve the catalytic activity. Noticeably, the OER current of Co_3O_4C-NA largely exceeds that of IrO_2/C (coated on Cu foil with the same loading amount and carbon content as that of Co_3O_4C-NA; see synthesis details in the Supporting Information), despite the slightly lower onset potential of IrO_2/C (~1.45 V), featuring much better catalytic performance of Co_3O_4C-NA.

We further compared the operating potentials required for different catalysts to deliver a 10.0 mA cm^{-2} current density ($E_{j=10}$), which is a metric related to solar fuel synthesis.[18] Co_3O_4C-NA affords a current density of 10.0 mA cm^{-2} at 1.52 V (Figure 3a), lower than that of IrO_2/C at 1.54 V and of many other reported noble-metal catalysts.[3b,5c,19] Moreover, this excellent OER activity of Co_3O_4C-NA is not only better than that of most of the state-of-the-art Co-based transition-metal electrocatalysts[4d,e,17a,18,20] and nonmetal catalysts[5] but also superior to that of all the nanowire array electrodes reported to date: i.e., $Zn_xCo_{3-x}O_4$ nanowire arrays grown on Ti foils (1.55 V, pH 14),[9a] $Ni_xCo_{3-x}O_4$ nanowire arrays grown on Ti foils (~1.60 V, pH 14),[9b] and Ni-substituted Co_3O_4 nanowire arrays grown on Ni foams (~1.60 V, pH 14).[11] A detailed comparison of different highly active OER catalysts with various electrode configurations is shown in Table S1 (Supporting Information), further confirming the outstanding catalytic behavior of Co_3O_4C-NA. In addition, the catalytic kinetics for oxygen evolution was examined by Tafel plots (Figure 3b). The Tafel slope value of Co_3O_4C-NA (70 mV $decade^{-1}$) is lower than those of the Co-based MOF (142 mV $decade^{-1}$) and IrO_2/C (97 mV $decade^{-1}$; Figure S7, Supporting Information) and comparable to that of the previously reported highly active OER catalysts (Table S1), suggesting its favorable reaction kinetics.

To investigate the reaction mechanism, the rotating ring-disk electrode (RRDE) technique was employed with a Pt ring electrode potential of 1.50 V to oxidize the peroxide intermediates formed at the Co_3O_4C-NA surface during OER. Co_3O_4C-NA was scraped off from Cu foil and coated on a RRDE (see experimental details in the Supporting Information). As shown in Figure 3c, a very low ring current (μA scale) was detected, which is 3 orders of magnitude lower than that of the disk current (mA scale), suggesting negligible hydrogen peroxide formation and therefore a desirable four-electron pathway for water oxidation: i.e., $4OH^- \rightarrow O_2 + 2H_2O + 4e^-$. Furthermore, to confirm that the observed current originates from water oxidation rather than other side reactions and to calculate the Faradaic efficiency, an RRDE with a ring potential of 0.40 V was applied to reduce the generated O_2, rendering a continuous OER (disk electrode) → ORR (ring electrode) process (Figure S8, Supporting Information). With the disk current held constant at 200 μA, O_2 molecules generated from the Co_3O_4C-NA catalyst surface on the disk electrode sweep across the surrounding Pt ring electrode that is held at an ORR potential and are rapidly reduced. Consequently, a ring current of ~39.7 μA (collection efficiency 0.2) was detected (Figure 3d), which verifies that the observed oxidation current catalyzed by Co_3O_4C-NA can be fully attributed to OER with a high Faradaic efficiency of 99.3% (see detailed calculations in the Supporting Information).

Strong durability toward OER is of great significance for energy conversion and storage systems. The chronoamperometric response demonstrates the high stability of Co_3O_4C-NA, showing a slight anodic current attenuation of 6.5% within 30 h, whereas IrO_2/C displays a 4.7 times larger current attenuation of 30.4% (Figure 3e; Figure S9, Supporting Information), indicating the apparent advantage of active materials directly grown on conductive substrates in comparison to the postcoated catalysts on electrodes, because the latter suffer from peeling off during the evolution of a large amount of O_2 gas.[3−5] The XRD pattern of the catalyst after a 30 h reaction shows no phase change in comparison to the fresh Co_3O_4C-NA (Figure S10, Supporting Information), which corroborates that the hybrid Co_3O_4-carbon nanowire arrays act as highly OER active and stable catalysts. In the chronopotentiometric response, Co_3O_4C-NA affords a nearly constant operating potential of 1.52 V to deliver a 10.0 mA cm^{-2} current density (Figure 3e inset), whereas the potential of IrO_2/C increases >15 mV within 4000 s, again revealing the stronger durability of Co_3O_4C-NA. Further, only 3.3% anodic current loss was observed for Co_3O_4C-NA after 3000 continuous potential cyclings at an accelerated scanning rate of 100 mV s^{-1} (Figure 3f), confirming that the catalyst is also highly stable to withstanding accelerated degradation.

The effective operation of electrocatalysts in concentrated electrolytes is a critical figure of merit for practical applications.[18] In 1.0 M KOH, the high activity of Co_3O_4C-NA is well preserved, showing a larger current density and much lower Tafel slope of 61 mV $decade^{-1}$ in comparison to that of IrO_2/C (87 mV $decade^{-1}$; Figure S11a,b, Supporting Information), indicating the superior reaction kinetics of Co_3O_4C-NA. Both the chronoamperometric and chronopotentiometric responses show much smaller OER activity attenuation of Co_3O_4C-NA in comparison to that of IrO_2/C (Figure S11c,d), demonstrating the strong durability of Co_3O_4C-NA in concentrated alkaline solutions.

The reaction reversibility initiated on an oxygen evolution electrode that can also efficiently catalyze the reverse ORR process, is of significant importance, especially for rechargeable metal−air batteries and regenerated fuel cells involving these two reactions. Thus, polarization curves were recorded in the whole region of OER and ORR. In the ORR region, Co_3O_4C-NA exhibits a half-wave potential ($E_{1/2}$) of 0.78 V (Figure 4)

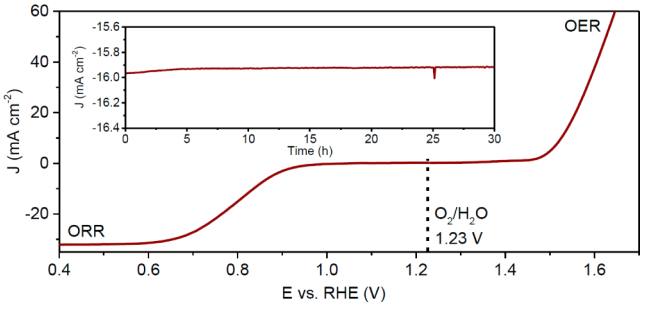

Figure 4. Polarization curve measured in O_2-saturated 0.1 M KOH solution (scan rate 0.5 mV s^{-1}) for Co_3O_4C-NA grown on Cu foil (directly used as the working electrode) in the whole region of OER and ORR. Inset: chronoamperometric response of Co_3O_4C-NA at a constant potential of 0.78 V ($E_{1/2}$), with methanol addition after 25 h.

dx.doi.org/10.1021/ja5082553 | J. Am. Chem. Soc. 2014, 136, 13925−13931

and Tafel slope of 89 mV decade^{-1} (Figure S12a, Supporting Information). The overall oxygen electrode activity can be evaluated by the difference of OER and ORR metrics ($\Delta E = E_{j=10} - E_{1/2}$). The smaller ΔE is, the closer the catalyst is to an ideal reversible oxygen electrode.[21] Co_3O_4C-NA exhibits a ΔE value of 0.74 V, lower than that of the recently reported highly active reversible oxygen electrodes, e.g. CoO/N-doped graphene (ΔE = 0.76 V),[20a] Co_3O_4/N-doped carbon (ΔE = 0.86 V),[21a] and H-Pt/$CaMnO_3$ (ΔE = 1.01 V),[21b] corroborating the excellent reversible oxygen electrode nature of Co_3O_4C-NA. Further, on combination of RRDE measurements that suggest an electron transfer number of 3.85−3.96 (from 0.40 to 0.90 V) for the ORR process (Figure S12b), Co_3O_4C-NA favors a desirable four-electron pathway for reversible OER and ORR. Moreover, Co_3O_4C-NA shows a strong durability for ORR, as revealed by the chronoamperometric response (Figure 4 inset), delivering a nearly constant current density within 30 h. Notably, the current density of Co_3O_4C-NA shows no obvious change even after the addition of methanol, indicating its high selectivity to ORR with strong methanol tolerance ability, which can avoid the poisoning crossover effect, displaying an important quality for cathode materials in low-temperature fuel cells.

2.3. Discussion. The unique hybrid nanowire composition and novel electrode configuration endow Co_3O_4C-NA with catalytic performance much better than that of conventional electrode materials. First, the in situ incorporation of carbon into Co_3O_4C-NA, assured by the use of a MOF as the precursor, leads to a structure with strongly interacting Co_3O_4 and carbon species (as evidenced by TEM, EDS, and XPS) and highly improved conductivity and charge transfer capability, which favor the high OER activity and stability. For the purpose of comparison, a carbon-free counterpart was prepared by calcination of Co_3O_4C-NA in air to eliminate carbon species (denoted as Co_3O_4-NA; see synthesis details in the Supporting Information), which also exhibits a porous nanowire array structure and a cubic spinel phase (Figures S3 and S13, Supporting Information) but affords a higher onset potential of 1.50 V, a larger operating potential of 1.64 V to deliver a 10.0 mA cm^{-2} current density (Figure 3a), and a higher Tafel slope of 123 mV decade^{-1} (Figure 3b) in comparison those of Co_3O_4C-NA, suggesting its much lower OER activity with inferior reaction kinetics. Also, the semicircular diameter in the electrochemical impedance spectrum (EIS) of Co_3O_4-NA is much larger than that of Co_3O_4C-NA, due to smaller contact and charge transfer impedance in Co_3O_4C-NA (Figure 5a). Notably, Co_3O_4C-NA also largely exceeds the physically mixed Co_3O_4-NA and carbon powder in OER performance (Figure 5b; see synthesis details in the Supporting Information), which implies that the outstanding activity of Co_3O_4C-NA with low resistance originates not simply from the increased electrical conductivity but also from a complex synergistic effect between strongly interacting Co_3O_4 and carbon species.[17] For instance, the in situ incorporated carbon causes the impaired electron density of Co atoms (as evidenced by XPS), which can make the catalytically active species (i.e., Co) more electrophilic, thus facilitating the adsorption and reaction of OH^- groups with Co_3O_4C-NA, resulting in enhanced OER activity in alkaline solutions.[22]

Second, the mesoporous nanowire arrays afford a large active surface area, which was evaluated by the electrochemical double-layer capacitance (C_{dl}) and surface roughness factor (R_f). By calculating the slope from the linear relationship of the

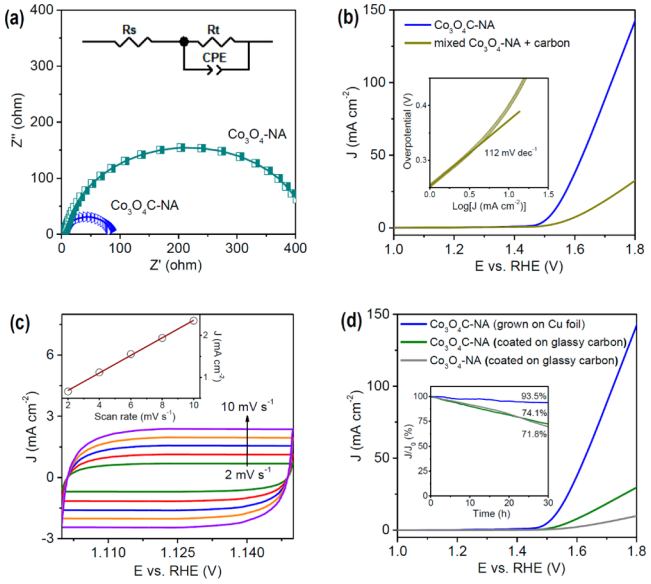

Figure 5. (a) EIS of Co_3O_4C-NA and Co_3O_4-NA recorded at 1.60 V. Inset in (a): the corresponding equivalent circuit diagram consisting of an electrolyte resistance (Rs), a charge-transfer resistance (Rt), and a constant-phase element (CPE). (b) Polarization curves of Co_3O_4C-NA directly grown on Cu foil and physically mixed Co_3O_4-NA and carbon powder coated on Cu foil. Inset in (b): Tafel plot of the physically mixed Co_3O_4-NA and carbon powder. (c) Cyclic voltammograms (CVs) of Co_3O_4C-NA measured at different scan rates from 2 to 10 mV s^{-1}. Inset in (c): plot of the current density at 1.14 V vs the scan rate. (d) Polarization curves of Co_3O_4C-NA directly grown on Cu foil and Co_3O_4C-NA and Co_3O_4-NA scraped off from Cu foil and coated on glassy-carbon electrodes. Inset in (d): the corresponding chronoamperometric response at a constant potential of 1.52 V.

current density against the scan rate (see calculation details in the Supporting Information), C_{dl} of Co_3O_4C-NA is confirmed to be 209.7 mF cm^{-2} with an R_f value of 3495 (Figure 5c), which is much higher than that of IrO_2/C (C_{dl} = 22.3 mF cm^{-2}, R_f = 371; Figure S14, Supporting Information). Since C_{dl} and R_f are proportional to the active surface area of electrocatalysts,[7−11] the results demostrate that mesoporous nanowire arrays directly grown on Cu foil are more effective in enlarging the catalytically active surface area in comparison to conventional planar catalyst films coated on electrodes; thus, better exposure and enhanced utilization of electroactive sites (e.g., Co species) on the large active surface of Co_3O_4C-NA greatly contribute to its ultrahigh OER activity.

Third, the reaction kinetics for OER is significantly promoted by the advanced electrode configuration. The nanowire arrays provide a smooth pathway for fast penetration of electrolyte, while the mesopores facilitate the access of reactants (e.g., OH^-) in the electrolyte to the active sites within nanowires, as well as the fast emission of reaction products (e.g., O_2). Accordingly, Co_3O_4C-NA displays a Tafel slope much smaller than that of IrO_2/C, physically mixed Co_3O_4-NA and carbon powder, and other catalysts in the control group (Figures 3b and 5b inset; Figures S7 and S11b, Supporting Information), indicating its more favorable reaction kinetics. In addition, its current density in the OER potential region is not susceptible to the scan rate, showing a variation of 3.5% (vs 14.3% of IrO_2/C) with an increase in the scan rate from 0.5 to 50 mV s^{-1} (Figure S15, Supporting Information), due to the improved mass transport in the mesoporous nanowire arrays.[5,7] Addi-

dx.doi.org/10.1021/ja5082553 | J. Am. Chem. Soc. 2014, 136, 13925−13931

tionally, the microstructure of nanowire arrays is believed to promote the release of evolved O_2 gas bubbles (Video S1, Supporting Information), by effectively bursting larger O_2 bubbles that commonly stick to the planar catalyst film surface and wicking the evolved bubbles to maintain the solid−liquid interface.[23]

Last but not least, the direct growth of active materials on the conductive Cu foil can greatly enhance the electron transport and adhesion between nanowire arrays and substrates, promote the structural stability for long-term usage, and avoid utilization of polymeric binders and extra conductive additives, consequently reducing the dead volume and undesirable interface in the electrode,[9−11,12b] which is corroborated by the much higher OER activity and stronger durability of Co_3O_4C-NA in comparison to those of IrO_2/C coated on Cu foil (Figure 3e) and those of Co_3O_4-NA and Co_3O_4C-NA scraped off from Cu foil and coated on traditional glassy-carbon electrodes (Figure 5d). Also, even on operation at the high potential of 1.80 V (delivering a very large current density of ∼140 mA cm^{-2}), Co_3O_4C-NA shows no visible peeling from Cu foil (Video S1, Supporting Information), suggesting the strong stability of this type of oxygen evolution electrode.

3. CONCLUSIONS

In summary, hybrid Co_3O_4-carbon porous nanowire arrays directly grown on Cu foil exhibit higher OER activity, more favorable kinetics, and stronger durability in comparison to those of IrO_2/C. The OER performance is the best among all the reported nanowire array electrodes and is better than that of most of the highly active noble-metal/transition-metal and nonmetal OER catalysts, which can be attributed to the porous nanowire array electrode configuration and in situ carbon incorporation, leading to enlarged active surface area, strong structural stability, and improved mass/charge transport. Considering their capability for catalyzing ORR through an efficient four-electron pathway, these new reversible oxygen electrodes are promising for direct use in metal−air batteries, fuel cells, water-splitting devices, and other key renewable energy systems.

■ ASSOCIATED CONTENT

Supporting Information

Text, figures, a table, a video, and CIF files giving experimental details, SEM images, crystalline structure, and N_2 adsorption of the Co-based MOF, XPS, XRD, and SEM images and N_2 adsorption of Co_3O_4-NA, optical photos of three-electrode OER testing cells, OER activity and stability tests of Co_3O_4C-NA in 1.0 M KOH, polarization curves, Tafel plots, and stability tests of control groups, Tafel plot, electron transfer number, and HO_2^- production curves for ORR of Co_3O_4C-NA, a detailed comparison of various OER catalysts, and Co_3O_4C-NA working at different operating potentials. This material is available free of charge via the Internet at http://pubs.acs.org.

■ AUTHOR INFORMATION

Corresponding Author

*E-mail for S.Z.Q.: s.qiao@adelaide.edu.au.

Author Contributions

All authors have given approval to the final version of the manuscript.

Notes

The authors declare no competing financial interest.

■ ACKNOWLEDGMENTS

This work was financially supported by the Australian Research Council (ARC) through the Discovery Project programs (DP140104062 and DP130104459).

■ REFERENCES

(1) (a) Kim, T. W.; Choi, K. S. *Science* **2014**, *343*, 990−994. (b) Zhang, M.; de Respinis, M.; Frei, H. *Nat. Chem.* **2014**, *6*, 362−367. (c) Yuan, C. Z.; Wu, H. B.; Xie, Y.; Lou, X. W. *Angew. Chem.* **2014**, *126*, 1512−1530; *Angew. Chem., Int. Ed.* **2014**, *53*, 1488−1504.

(2) (a) Katsounaros, I.; Cherevko, S.; Zeradjanin, A. R.; Mayrhofer, K. J. J. *Angew. Chem.* **2014**, *126*, 104−124; *Angew. Chem., Int. Ed.* **2014**, *53*, 102−121. (b) Oh, S. H.; Black, R.; Pomerantseva, E.; Lee, J. H.; Nazar, L. F. *Nat. Chem.* **2012**, *4*, 1004−1010.

(3) (a) Over, H. *Chem. Rev.* **2012**, *112*, 3356−3426. (b) Lee, Y.; Suntivich, J.; May, K. J.; Perry, E. E.; Shao-Horn, Y. *J. Phys. Chem. Lett.* **2012**, *3*, 399−404.

(4) (a) Jin, K.; Park, J.; Lee, J.; Yang, K. D.; Pradhan, G. K.; Sim, U.; Jeong, D.; Jang, H. L.; Park, S.; Kim, D.; Sung, N. E.; Kim, S. H.; Han, S.; Nam, K. T. *J. Am. Chem. Soc.* **2014**, *136*, 7435−7443. (b) Gong, M.; Li, Y. G.; Wang, H. L.; Liang, Y. Y.; Wu, J. Z.; Zhou, J. G.; Wang, J.; Regier, T.; Wei, F.; Dai, H. J. *J. Am. Chem. Soc.* **2013**, *135*, 8452−8455. (c) Subbaraman, R.; Tripkovic, D.; Chang, K. C.; Strmcnik, D.; Paulikas, A. P.; Hirunsit, P.; Chan, M.; Greeley, J.; Stamenkovic, V.; Markovic, N. M. *Nat. Mater.* **2012**, *11*, 550−557. (d) Gao, M. R.; Xu, Y. F.; Jiang, J.; Zheng, Y. R.; Yu, S. H. *J. Am. Chem. Soc.* **2012**, *134*, 2930−2933. (e) Liang, Y. Y.; Li, Y. G.; Wang, H. L.; Zhou, J. G.; Wang, J.; Regier, T.; Dai, H. J. *Nat. Mater.* **2011**, *10*, 780−786.

(5) (a) Ma, T. Y.; Dai, S.; Jaroniec, M.; Qiao, S. Z. *Angew. Chem.* **2014**, *126*, 7409−7413; *Angew. Chem., Int. Ed.* **2014**, *53*, 7281−7285. (b) Tian, G. L.; Zhao, M. Q.; Yu, D.; Kong, X. Y.; Huang, J. Q.; Zhang, Q.; Wei, F. *Small* **2014**, *10*, 2251−2259. (c) Zhao, Y.; Nakamura, R.; Kamiya, K.; Nakanishi, S.; Hashimoto, K. *Nat. Commun.* **2013**, *4*, 2390. (d) Park, H. W.; Lee, D. U.; Liu, Y.; Wu, J.; Nazar, L. F.; Chen, Z. *J. Electrochem. Soc.* **2013**, *160*, A2244−A2250.

(6) (a) Wang, J.; Zhong, H. X.; Qin, Y. L.; Zhang, X. B. *Angew. Chem.* **2013**, *125*, 5356−5361; *Angew. Chem., Int. Ed.* **2013**, *52*, 5248−5253. (b) Xin, S.; Guo, Y. G.; Wan, L. J. *Acc. Chem. Res.* **2012**, *45*, 1759−1769. (c) Cheng, F. Y.; Chen, J. *Chem. Soc. Rev.* **2012**, *41*, 2172−2192. (d) Kibsgaard, J.; Gorlin, Y.; Chen, Z.; Jaramillo, T. F. *J. Am. Chem. Soc.* **2012**, *134*, 7758−7765. (e) Lang, X. Y.; Hirata, A.; Fujita, T.; Chen, M. W. *Nat. Nanotechnol.* **2011**, *6*, 232−236.

(7) (a) Wang, K.; Wu, H.; Meng, Y.; Wei, Z. *Small* **2014**, *10*, 14−31. (b) Shen, L.; Che, Q.; Li, H.; Zhang, X. *Adv. Funct. Mater.* **2014**, *24*, 2630−2637. (c) Jiang, Y.; Zhang, X.; Ge, Q. Q.; Yu, B. B.; Zou, Y. G.; Jiang, W. J.; Song, W. G.; Wan, L. J.; Hu, J. S. *Nano Lett.* **2014**, *14*, 365−372. (d) Tian, J. Q.; Liu, Q.; Asiri, A. M.; Sun, X. P. *J. Am. Chem. Soc.* **2014**, *136*, 7587−7590. (e) Liao, J. Y.; Higgins, D.; Lui, G.; Chabot, V.; Xiao, X.; Chen, Z. *Nano Lett.* **2013**, *13*, 5467−5473. (f) Yuan, C.; Yang, L.; Hou, L.; Shen, L.; Zhang, X.; Lou, X. W. *Energy Environ. Sci.* **2012**, *5*, 7883−7887.

(8) (a) Jiang, J.; Li, Y.; Liu, J.; Huang, X.; Yuan, C.; Lou, X. W. *Adv. Mater.* **2012**, *24*, 5166−5180. (b) Gong, K.; Du, F.; Xia, Z.; Durstock, M.; Dai, L. M. *Science* **2009**, *323*, 760−764.

(9) (a) Liu, X. J.; Chang, Z.; Luo, L.; Xu, T. H.; Lei, X. D.; Liu, J. F.; Sun, X. M. *Chem. Mater.* **2014**, *26*, 1889−1895. (b) Li, Y.; Hasin, P.; Wu, Y. *Adv. Mater.* **2010**, *22*, 1926−1929.

(10) Lee, D. U.; Choi, J. Y.; Feng, K.; Park, H. W.; Chen, Z. *Adv. Energy Mater.* **2014**, *4*, 1301389.

(11) Lu, B.; Cao, D.; Wang, P.; Wang, G.; Gao, Y. *Int. J. Hydrogen Energy* **2011**, *36*, 72−78.

(12) (a) Artero, V.; Chavarot-Kerlidou, M.; Fontecave, M. *Angew. Chem.* **2011**, *123*, 7376−7405; *Angew. Chem., Int. Ed.* **2011**, *50*, 7238−7266. (b) Cui, B.; Lin, H.; Li, J. B.; Li, X.; Yang, J.; Tao, J. *Adv. Funct. Mater.* **2008**, *18*, 1440−1447.

(13) (a) Sun, J. K.; Xu, Q. *Energy Environ. Sci.* **2014**, *7*, 2071−2100. (b) Proietti, E.; Jaouen, F.; Lefèvre, M.; Larouche, N.; Tian, J.; Herranz, J.; Dodelet, J. P. *Nat. Commun.* **2011**, *2*, 416. (c) Furukawa,

H.; Cordova, K. E.; O'Keeffe, M.; Yaghi, O. M. *Science* **2013**, *341*, 1230444.
(14) Kaduk, J. A.; Hanko, J. A. *J. Appl. Crystallogr.* **2001**, *34*, 710−714.
(15) Gu, D.; Schüth, F. *Chem. Soc. Rev.* **2014**, *43*, 313−344.
(16) Banerjee, D.; Jagadeesh, R. V.; Junge, K.; Pohl, M. M.; Radnik, J.; Brückner, A.; Beller, M. *Angew. Chem.* **2014**, *126*, 4448−4452; *Angew. Chem., Int. Ed.* **2014**, *53*, 4359−4363.
(17) (a) Wu, J.; Xue, Y.; Yan, X.; Yan, W.; Cheng, Q.; Xie, Y. *Nano Res.* **2012**, *5*, 521−530. (b) Li, J.; Tang, S. B.; Lu, L.; Zeng, H. C. *J. Am. Chem. Soc.* **2007**, *129*, 9401−9409.
(18) McCrory, C. C. L.; Jung, S.; Peters, J. C.; Jaramillo, T. F. *J. Am. Chem. Soc.* **2013**, *135*, 16977−16987.
(19) Mamaca, N.; Mayousse, E.; Arrii-Clacens, S.; Napporn, T. W.; Servat, K.; Guillet, N.; Kokoh, K. B. *Appl. Catal. B: Environ.* **2012**, *111*−*112*, 376−380.
(20) (a) Mao, S.; Wen, Z.; Huang, T.; Hou, Y.; Chen, J. *Energy Environ. Sci.* **2014**, *7*, 609−616. (b) Zou, X.; Goswami, A.; Asefa, T. *J. Am. Chem. Soc.* **2013**, *135*, 17242−17245. (c) Smith, R. D. L.; Prévot, M. S.; Fagan, R. D.; Trudel, S.; Berlinguette, C. P. *J. Am. Chem. Soc.* **2013**, *135*, 11580−11586.
(21) (a) Masa, J.; Xia, W.; Sinev, I.; Zhao, A.; Sun, Z.; Grützke, S.; Weide, P.; Muhler, M.; Schuhmann, W. *Angew. Chem.* **2014**, *126*, 8648−8652; *Angew. Chem., Int. Ed.* **2014**, *53*, 8508−8512. (b) Han, X. P.; Cheng, F. Y.; Zhang, T. R.; Yang, J. G.; Hu, Y. X.; Chen, J. *Adv. Mater.* **2014**, *26*, 2047−2051.
(22) Lu, Z.; Wang, H.; Kong, D.; Yan, K.; Hsu, P. C.; Zheng, G.; Yao, H.; Liang, Z.; Sun, X.; Cui, Y. *Nat. Commun.* **2014**, *5*, 4345.
(23) (a) Kong, D.; Wang, H.; Lu, Z.; Cui, Y. *J. Am. Chem. Soc.* **2014**, *136*, 4897−4900. (b) Faber, M. S.; Dziedzic, R.; Lukowski, M. A.; Kaiser, N. S.; Ding, Q.; Jin, S. *J. Am. Chem. Soc.* **2014**, *136*, 10053−10061.